

# Genuine multipartite entanglement in a one-dimensional Bose-Hubbard model with frustrated hopping

Sudipto Singha Roy,<sup>1,2</sup> Leon Carl,<sup>1</sup> and Philipp Hauke<sup>1,2</sup>

<sup>1</sup>*Pitaevskii BEC Center, CNR-INO and Dipartimento di Fisica, Università di Trento, I-38123 Trento, Italy*

<sup>2</sup>*INFN-TIFPA, Trento Institute for Fundamental Physics and Applications, Trento, Italy*

(Dated: December 1, 2022)

Frustration and quantum entanglement are two exotic quantum properties in quantum many-body systems. However, despite several efforts, an exact relation between them remains elusive. In this work, we explore the relationship between frustration and quantum entanglement in a physical model describing strongly correlated ultracold bosonic atoms in optical lattices. In particular, we consider the one-dimensional Bose-Hubbard model comprising both nearest-neighbor ( $t_1$ ) and frustrated next-nearest neighbor ( $t_2$ ) hoppings and examine how the interplay of onsite interaction ( $U$ ) and hoppings results in different quantum correlations dominating in the ground state of the system. We then analyze the behavior of quantum entanglement in the model. In particular, we compute genuine multipartite entanglement as quantified through the generalized geometric measure and make a comparative study with bipartite entanglement and other relevant order parameters. We observe that genuine multipartite entanglement has a very rich behavior throughout the considered parameter regime and frustration does not necessarily favor generating a high amount of it. Moreover, we show that in the region with strong quantum fluctuations, the particles remain highly delocalized in all momentum modes and share a very low amount of both bipartite and multipartite entanglement. Our work illustrates the necessity to give separate attention to dominating ordering behavior and quantum entanglement in the ground state of strongly correlated systems.

## I. INTRODUCTION

The past few decades have witnessed many interesting theoretical developments in the field of quantum information theory. On one hand, the laws of quantum mechanics have been exploited to propose quantum computation and quantum information schemes that often surpass their classical counterparts [1–8]. On the other hand, tools from quantum information theory have been used to unveil many interesting phenomena of physical systems that belong to a wide variety of interdisciplinary fields, ranging from condensed matter systems [9–13] over high-energy physics [14–17] to holography [18–23], etc. In recent years, promising developments have been reported in designing state-of-the-art quantum technologies using quantum many-body systems that include trapped ions [24–27], superconducting quantum circuits [28–31], silicon-based devices [32–35], photonic systems [36–41], and atomic systems [42–44], which can efficiently produce large amounts of entanglement [45–49]. As in many cases quantum entanglement remains the key resource of quantum technologies, a primary step in the assessment of a quantum device demands complete characterization of its entanglement properties. Besides this, in the literature, there have been a plethora of works [9–12, 50–57] where alongside conventional order parameters, quantum entanglement has been considered as an efficient detector of quantum phase boundaries in exotic quantum many-body systems.

Quantum entanglement shared between a large number of parties often gives rise to a highly intricate form of quantum correlations, namely, multipartite entanglement (ME) [56–68]. It is known that ME can serve as a resource in the implementation of novel quantum schemes

such as measurement-based quantum computation [69], quantum cryptography [70], quantum sensing [71, 72], quantum error correction [73], etc. Moreover, there are instances where ME performs as a better identifier of quantum phase boundaries than bipartite entanglement (BE) [74–76]. However, quantification of ME in complex quantum many-body systems is an extremely challenging task. Unlike BE, a computable measure of ME is difficult to construct even for pure quantum states. In particular, the characterization of genuine multipartite entanglement (GME) requires full knowledge of the entanglement distribution in all possible bipartitions of the system [56, 58–61, 64, 77]. Hence, a complete characterization of ME even for a finite-size system is an important albeit difficult task.

In this work, we consider one paradigmatic model of strongly correlated quantum particles on an optical lattice, namely the Bose-Hubbard model [78–80] with frustration which is introduced by the inclusion of beyond nearest-neighbor hopping (Fig. 1(a)), and characterize its bipartite and multipartite entanglement properties. The limiting cases of the model have been well explored in previous works. For instance, in the hard-core boson limit in the ground state (GS) configuration, there exists a competition between vector chiral and several dimer orders resulting from strong quantum fluctuations [81–84]. In contrast, near the limit of vanishing onsite interaction, the quantum phase reminiscent to the classical spin spiral phase remains a dominating feature of the GS. In our work, we aim to explore how the GS characteristics change as a result of the interplay of finite onsite interaction interpolating between the two limiting cases and frustration in the system. In particular, we aim at identifying regions in the parameter space comprising different

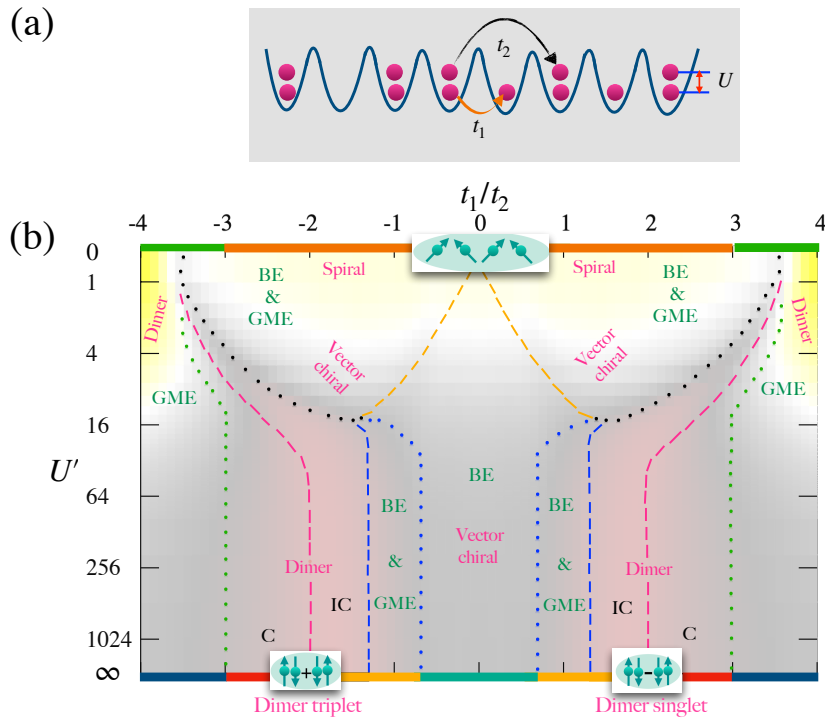


Figure 1. (a) Schematic of arrangement of quantum particles in a one-dimensional (1D) lattice described by the Bose–Hubbard model comprising NN ( $t_1$ ) and NNN ( $t_2$ ) hoppings and onsite interaction  $U$ . Competition between those parameters leads to frustration and strong quantum fluctuations. (b) We schematically show the distribution of different dominating quantum correlations in the GS of the above Bose–Hubbard model, in the  $U' - t_1/t_2$  plane. Here, using the analysis performed in Sec. III B and III C, we mark the regions with different dominating orders and use dotted lines to approximately separate them. The subsequent analysis of quantum entanglement presented in Sec. IV helps us in identifying the regions with dominating genuine multipartite entanglement (GME) and bipartite entanglement (BE), quantified through generalized geometric measure and half-chain entanglement entropy, respectively. For small  $U$ , the dashed yellow and dotted black lines enclose the region with both high BE and GME. Similar region for high  $U$  is marked by the dashed and dotted blue lines. Additionally, we draw the approximate boundary (dashed magenta lines) separating predominating commensurate (C) and incommensurate (IC) phase orderings as discussed in Sec. III A.

ordering tendencies and make a comparative study with the entanglement properties. As a measure of GME, we consider the generalized geometric measure (GGM) [58–61, 64] and observe its rich behavior in the considered parameter regime. For a wide region in the parameter space, the behavior of both BE and GME remain compatible with that of chiral order in that region. However, unlike BE, when NNN hopping dominates ( $|t_1|/t_2 < 1$ ), GME becomes very low. In contrast, in the region where strong quantum frustration drives the system to assume dimer order, we observe a significantly lower value of both BE and GME. Based on our analysis, we argue that the behavior obtained for the hard-core boson limit of the model approximately translates up to a finite but moderate value of onsite interaction. Moreover, our work suggests entanglement properties of quantum many-body systems do not always manifest in the behavior of different ordering tendencies and deserve separate analysis.

The article is organized as follows. In Sec. II, we introduce the model Hamiltonian that we consider in our work and discuss its two limiting cases. In Sec. III, we discuss

the behavior of different order parameters obtained for the GS of the model, leading to the sketch displayed in Fig. 1(b). Thereafter, in Sec. IV, we discuss the entanglement properties of the model and compare them with the results obtained in Sec. III. We finally conclude and discuss our future plans in Sec. V.

## II. MODEL

In this section, we introduce the model Hamiltonian that we consider in our work, which is the Bose–Hubbard (BH) model in 1D with both nearest-neighbor (NN) and next-nearest-neighbor (NNN) tunneling terms, given by

$$\hat{H} = -t_1 \sum_{\langle i,j \rangle} (\hat{b}_i^\dagger \hat{b}_j + \hat{b}_j^\dagger \hat{b}_i) - t_2 \sum_{\langle\langle i,j \rangle\rangle} (\hat{b}_i^\dagger \hat{b}_j + \hat{b}_j^\dagger \hat{b}_i) + \frac{U}{2} \sum_i \hat{n}_i (\hat{n}_i - 1), \quad (1)$$

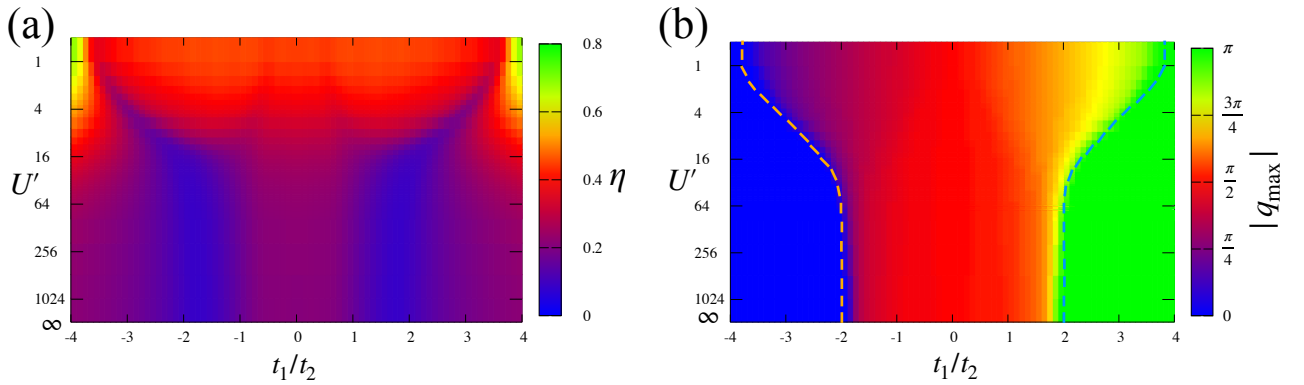


Figure 2. Variation of momentum density in the GS of the Bose-Hubbard model with the NN and NNN hopping ratio and contact interaction. (a) Behavior of maximum occupation density  $\eta = \max_q \langle \hat{b}_q^\dagger \hat{b}_q \rangle / N$  obtained for OBC. For moderately large values of  $U$ ,  $\eta$  takes its minimal value in the region  $1 < |t_1|/t_2 < 2$ . This suggests the bosons are delocalized or maximally spread over all momentum modes, indicating regions with strong quantum fluctuations. For small  $U$  and PBC, bosons condense into a single mode (collinear phases at  $|t_1|/t_2 > 4$ ) or two modes (spiral phase). We denote the maximally populated momentum mode by  $q_{\max}$  and plot it in panel (b). At  $U \rightarrow 0$ , it minimizes the dispersion relation given in Eq. (4). The dashed yellow (blue) line (Lifshitz line) distinguishes the regions with predominating commensurate phase order observed for  $q_{\max} = 0$  ( $|q_{\max}| = \pi$ ) and the noncommensurate phase order observed for  $0 < |q_{\max}| < \frac{\pi}{2}$  ( $\frac{\pi}{2} < |q_{\max}| < \pi$ ). Data for  $N = 10$  and  $M = 20$ .

where  $\hat{b}_i$  is the bosonic annihilation operator at site  $i$ ,  $t_1$  ( $t_2$ ) corresponds to the NN (NNN) hopping amplitude,  $U$  is the on-site interaction energy, and  $n_i$  is the number of bosons at site  $i$ . The total number of sites is given by  $M$  and  $N = \sum_i n_i$  denotes the number of particles. Physically, such a model may be realized in an optical lattice in a zig-zag ladder configuration [80, 85], where  $t_1/t_2$  can be tuned via the ladder width. The sign of  $t_1/t_2$  can be adjusted through a synthetic magnetic field [86–91].

Before going into details of our analysis, we review two limiting cases of the model.

### A. Free bosons, $U = 0$ limit

For the  $U = 0$  limit, and periodic boundary conditions (PBC), the following relation

$$\hat{b}_j = \frac{1}{\sqrt{M}} \sum_q e^{ijq} \hat{b}_q, \quad (2)$$

diagonalizes the above Hamiltonian to

$$\hat{H} = \sum_q \mathcal{E}_q \hat{b}_q^\dagger \hat{b}_q. \quad (3)$$

The dispersion relation in this free-boson limit is given by

$$\mathcal{E}_q = -2t_1 \cos q - 2t_2 \cos 2q. \quad (4)$$

Depending on the sign of  $t_2$ , two distinct regimes appear:

i) For  $t_2 > 0$ :  $\mathcal{E}_q$  is minimized by having all atoms in the  $q = 0$  mode, for  $t_1 > 0$  ( $q = \pi$  mode, for  $t_1 < 0$ ).

ii) For  $t_2 < 0$ : There is a competition between the first and second term in  $\mathcal{E}_q$ , which independently would be minimized by  $q = 0$  for  $t_1 > 0$  ( $q = \pi$ , for  $t_1 < 0$ ) and  $q = \pm\pi/2$ , respectively. As a result, the maximally populated  $q$  mode that yields minimum  $\mathcal{E}_q$  becomes

$$q_{\max} = \begin{cases} 0, & \text{for } t_1/t_2 \leq -4, \\ \pm \cos^{-1}(-\frac{t_1}{4t_2}), & \text{for } -4 < t_1/t_2 < 4, \\ \pi, & \text{for } t_1/t_2 \geq 4. \end{cases} \quad (5)$$

Hence,  $q_{\max}$  behaves exactly as the pitch angle of the helical spin arrangements of the corresponding frustrated classical spin model.

In our analysis, we consider the second scenario, and the primary focus will be in the region  $-4 \leq t_1/t_2 \leq 4$ , that consists of a ferromagnetic phase for  $t_1/t_2 < -4$ , a classical spiral phase for  $-4 < t_1/t_2 < 4$ , and an antiferromagnetic phase for  $t_1/t_2 > 4$ . To mitigate the effect of incommensurate pitch angles in our finite-size numerics, in the remainder of this work we consider open boundary conditions (OBC). One should note that when we consider  $U \neq 0$  or OBC, the above dispersion relation will not reflect the actual GS population and we expect the particles to occupy other momentum modes as well.

### B. Hard-Core Bosons, $U \rightarrow \infty$ limit: mapping to $J_1$ - $J_2$ -model

In the limit  $U \rightarrow \infty$ , the occupation of bosons per site is limited to  $\max_i \{n_i\} = 1$ . Hence, we can map the Bose-Hubbard model to a spin-1/2 system. One way to do that

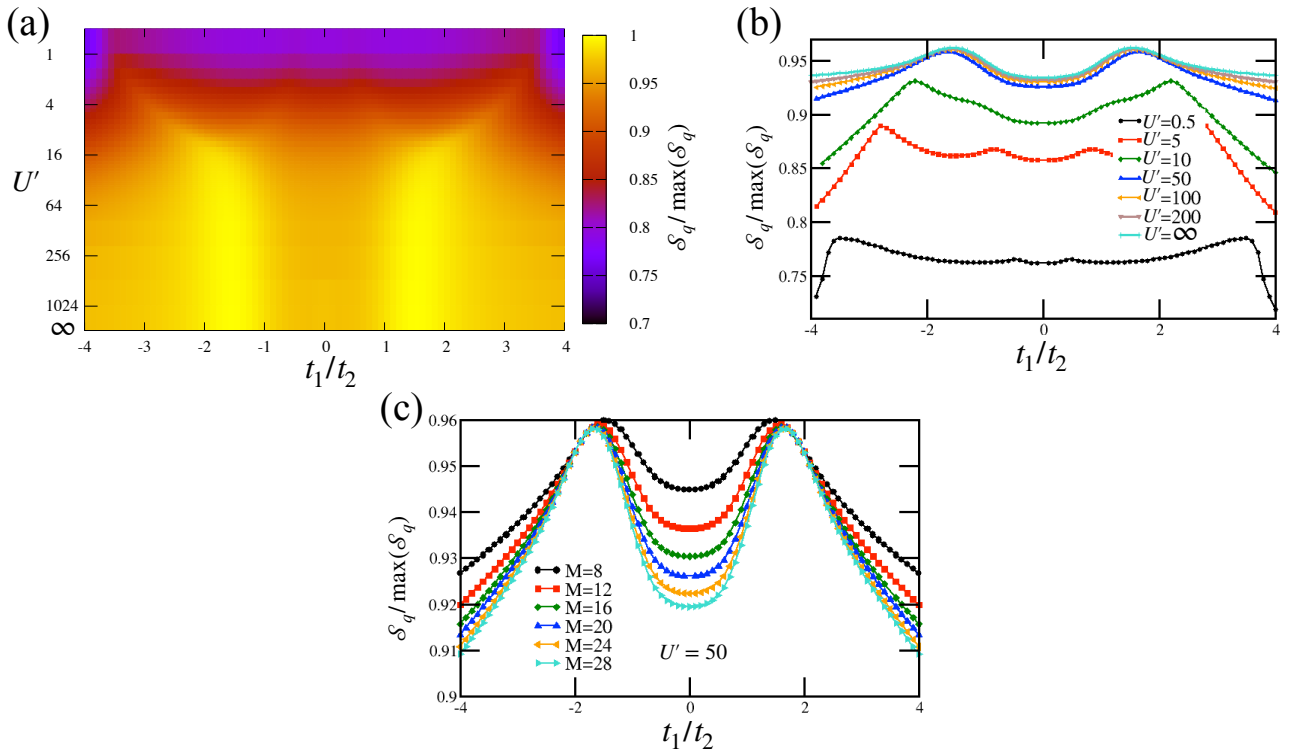


Figure 3. Spread of population of quantum particles across different momentum modes. (a) Entropy of momentum population in GS, as quantified by  $\mathcal{S}_q$  for  $N = 10$ ,  $M = 20$ . In the plot, we scaled  $\mathcal{S}_q$  by its maximum value  $\max(\mathcal{S}_q) = \ln N_q$ . (b) Cuts of  $\mathcal{S}_q$  for fixed  $U$ , for  $N = 10$ , and  $M = 20$ . In panel (c), we plot the scaling of  $\mathcal{S}_q / \max(\mathcal{S}_q)$  with different system sizes,  $M = 8, 12, 16, 20, 24$ , and  $28$  for  $U' = 50$ . The scaling suggests even at moderate system size  $\mathcal{S}_q / \max(\mathcal{S}_q)$  tends to converge to a large value in the region  $t_1/t_2 = \pm 2$ , indicating increased quantum fluctuations.

is following the Holstein–Primakoff transformation [92]

$$\hat{S}^+ = \sqrt{2s} \sqrt{1 - \frac{\hat{n}}{2s}} \hat{b} \approx \hat{b}, \quad (6)$$

where  $s$  is the spin of the particles, and similar for  $\hat{S}^-$ . In the limit  $U \rightarrow \infty$ , the relation in Eq. (6) becomes exact. With this transformation, the BH model with NNN-tunneling maps to

$$\begin{aligned} \hat{H} &\approx -t_1 \sum_{\langle i,j \rangle} \left( \hat{S}_i^- \hat{S}_j^+ + h.c. \right) - t_2 \sum_{\langle\langle i,j \rangle\rangle} \left( \hat{S}_i^- \hat{S}_j^+ + h.c. \right), \\ &= J_1 \sum_{\langle i,j \rangle} \left( \hat{S}_i^x \hat{S}_j^x + \hat{S}_i^y \hat{S}_j^y \right) + J_2 \sum_{\langle\langle i,j \rangle\rangle} \left( \hat{S}_i^x \hat{S}_j^x + \hat{S}_i^y \hat{S}_j^y \right), \end{aligned} \quad (7)$$

with  $\hat{S}_i^x = \frac{\hat{S}_i^+ + \hat{S}_i^-}{2}$ ,  $\hat{S}_i^y = \frac{\hat{S}_i^+ - \hat{S}_i^-}{2i}$ ,  $J_1 = -2t_1$ , and  $J_2 = -2t_2$ . The transformed Hamiltonian is the well-known  $XX$ -model with NN- and NNN-interactions also commonly known as the  $J_1$ - $J_2$  model. From earlier works [83, 84], it is known that for  $0 \leq |J_1|/J_2 \leq 4$ , there exist three regions, namely, Tomonaga-Luttinger liquid (TLL) phase, even- or odd-dimer phase, and vector chiral phase.

### III. RESULTS

In our work, our main focus will be on the intermediate values of  $U$ . In other words, we wish to find how different orders in the system change in presence of finite but nonzero  $U$ . Towards that aim, we compute a list of quantities and order parameters, using numerically exact diagonalization as well as tensor-network methods by employing the density matrix normalizing group [93] technique. Here, for all computational purposes we consider the system at half-filling,  $N = M/2$ , and we set  $t_2 = -1$ . Additionally, we denote  $U' = U/|t_2|$ .

#### A. Population in momentum modes

In Fig. 2(a), we plot the maximum bosonic density  $\eta = \max_q n_q / N$  (with  $n_q = 1/M \sum_{ij} e^{-iq(i-j)} \langle \hat{b}_i^\dagger \hat{b}_j \rangle$ ) in the GS. In panel (b), we plot the corresponding momentum mode with maximum population,  $q_{\max}$ .  $\eta$  is also known as the structure factor of the system, and a nonzero value of it in the thermodynamic limit guarantees presence of long-range order (LRO) at the wave vector  $q_{\max}$ . As here we are considering OBC,  $q$  is no longer a good quantum number and it can take any continuous value in between

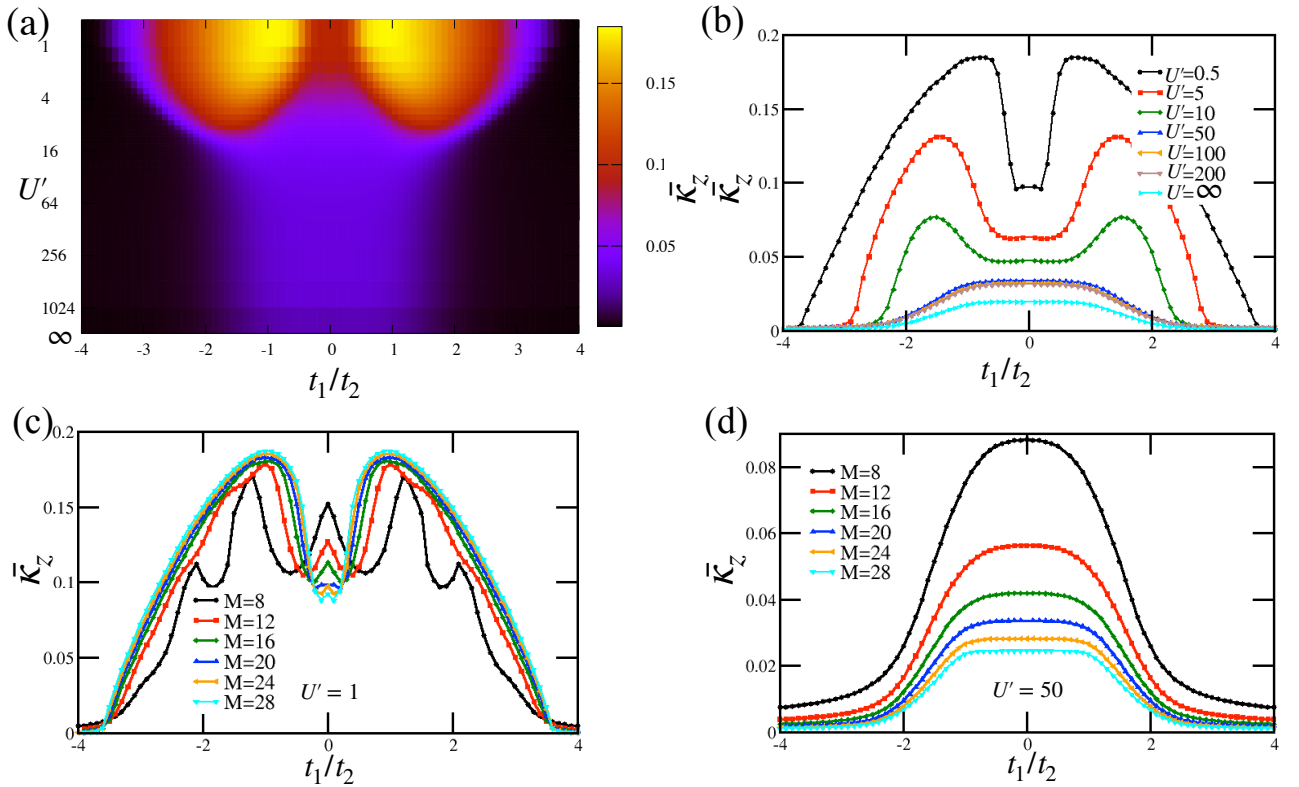


Figure 4. (a) Behavior of chiral order parameter  $\bar{\kappa}_z$  for system size  $N = 10$ ,  $M = 20$ . (b) Scaling of  $\bar{\kappa}_z$  with different values of onsite interaction  $U$ , and for the same system size as in panel (a). In panel (c) and (d), we provide a finite-size scaling of  $\bar{\kappa}_z$  with system size  $M = 8, 12, 16, 20, 24$ , and  $28$ , for two values of onsite interactions,  $U = 1$  and  $50$ , respectively. The finite-size scaling analysis shows with the increasing system size  $\bar{\kappa}_z$  tends to converge in all the considered regions. At small  $U$ , it remains finite in the region  $|t_1/t_2| \lesssim 4$ , corresponding to the spiral phase at  $U \rightarrow 0$  whereas for large  $U$  this region shrinks to  $|t_1/t_2| \lesssim 2$ .

$q \in (-\pi, \pi]$ , which helps to alleviate incommensurability effects appearing in the frustrated system due to finite system size. In our analysis, we took  $N_q = 10^3$  values of  $q$  (with a difference  $\Delta_q \pi$ ).

From Fig. 2(a), we can see that the GS population density is maximum near  $U \rightarrow 0$  and  $|t_1/t_2| \sim 4$ . With the increase of  $U$ , bosons no longer condense into a single mode and  $\eta$  becomes minimal approximately in the region  $1 < |t_1/t_2| < 2$ . Moreover, the maximally populated mode  $q_{\max}$  broadly divides the region  $-4 \leq t_1/t_2 < 0$  (equivalently,  $0 < t_1/t_2 \leq 4$ ) into two parts: a region with predominant (i) commensurate (C) order  $q_{\max} = 0$  ( $q_{\max} = \pi$ ) and (ii) an incommensurate (IC) order  $0 < |q_{\max}| < \frac{\pi}{2}$  ( $\frac{\pi}{2} < |q_{\max}| < \pi$ ). We denote the transition by a dashed yellow (blue) line in Fig. 2(b), which is also known as the Lifshitz line [83, 84]. Comparing with the behavior of  $\eta$ ,  $q_{\max}$  indicates the pitch vector of dominating phase order, but not necessarily (quasi-)LRO.

Apart from the maximum population of the modes, the distribution of the particles among all the modes can give us a more detailed structure of the GS of the Hamiltonian. For that purpose, we compute the quantity  $\mathcal{S}_q = -\sum_q \rho_q \ln \rho_q$ , where  $\rho_q = n_q \Delta_q$ . Here, the factor  $\Delta_q$  ensures normalization  $\sum_q \rho_q = 1$ . We plot the be-

havior of  $\mathcal{S}_q / \max(\mathcal{S}_q)$  in Fig. 3, where  $\max(\mathcal{S}_q)$  is the theoretical maximum obtained at  $\rho_q = 1/N_q$ .  $\mathcal{S}_q$  reflects the structures predicted by  $\eta$ .

As discussed earlier, with increase of the contact interaction  $U$ , the GS starts populating other momentum modes, resulting in a high value of  $\mathcal{S}_q$  for the region  $1 < |t_1/t_2| < 2$ . A high value of  $\mathcal{S}_q$  in this context implies stronger quantum fluctuations and reduction of phase order, which is consistent with the behavior observed in the hard-core boson limit, where  $\mathcal{S}_q$  remains significantly high for the dimer phase and becomes maximum at  $|t_1/t_2| \approx 2$ ; see the scaling of  $\mathcal{S}_q / \max(\mathcal{S}_q)$  with  $U$  presented in Fig. 3(b). Additionally, we provide a finite-size scaling of  $\mathcal{S}_q / \max(\mathcal{S}_q)$  with  $M$  in Fig. 3(c) that suggests  $\mathcal{S}_q / \max(\mathcal{S}_q)$  tends to converge in the region  $t_1/t_2 = \pm 2$  even at moderately high system size. As we will see below, it is in these regions where the GS of the system comprises strong quantum fluctuations, leading to quantum phases without classical analog, in particular dimerized phases.

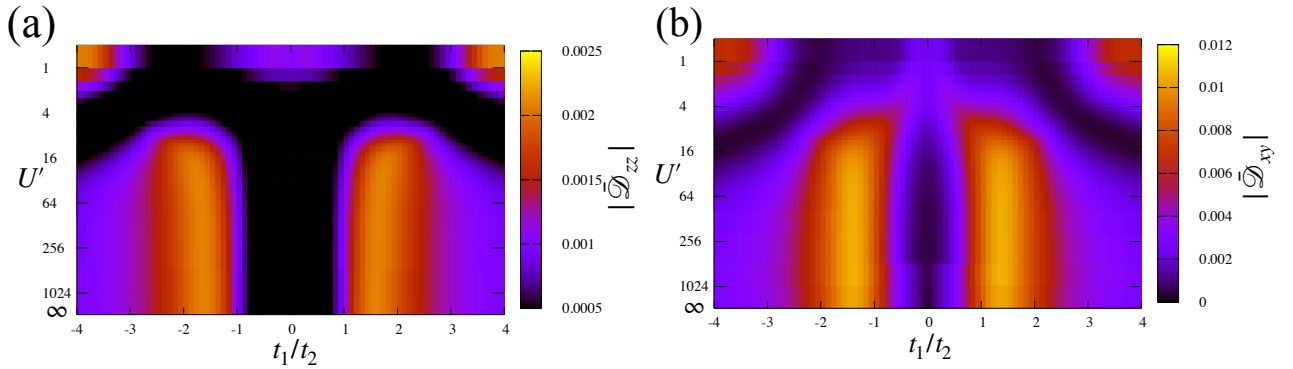


Figure 5. Dimer correlators obtained for the GS of the model. (a) Dimer  $zz$  correlator  $|\bar{\mathcal{D}}_{zz}|$  and (b) dimer  $xy$  correlator  $|\bar{\mathcal{D}}_{xy}|$  for  $N = 10$ ,  $M = 20$ . For a large portion in the parameter space, both the quantities remain significantly low. However, in the region  $1 < |t_1|/t_2 < 3$ , i.e., in the region with strong quantum fluctuations, both of them possess high values.

### B. Vector chiral order

To further understand the nature of the quantum phases appearing in the model, we consider as order parameter the chiral correlator, which measures chiral correlations between sites that are separated by a distance  $\Delta$  [82, 94], given by

$$\kappa_z^\Delta = \sum_{j=1}^{M-1-|\Delta|} \langle \kappa_j^z \kappa_{j+\Delta}^z \rangle. \quad (8)$$

Here  $\kappa_j^z = \frac{1}{2i}(\hat{b}_j^\dagger \hat{b}_{j+1} - \hat{b}_{j+1}^\dagger \hat{b}_j)$ , which using the spin-1/2 operators can also be written as  $\kappa_j^z = (\mathbf{S}_j \times \mathbf{S}_{j+1})^z$ . In addition, we also define the average of  $\kappa_z^\Delta$  over  $\Delta$ ,

$$\bar{\kappa}_z = \frac{1}{2M-3} \sum_{\Delta=-(M-2)}^{M-2} \frac{\kappa_z^\Delta}{M-1-|\Delta|}. \quad (9)$$

A nonzero value of  $\bar{\kappa}_z$  in the thermodynamic limit certifies the presence of long-range chiral order in the system. We present the behavior of  $\bar{\kappa}_z$  in Fig. 4(a), for  $M = 20$ . Near  $U \rightarrow 0$ ,  $\bar{\kappa}_z$  remains significantly high which is reminiscent of the classical spin spiral phase appearing in this region. As we increase  $U$  further, we can see  $\bar{\kappa}_z$  can distinguish the predominating commensurate phase order ( $q_{\max} = 0$  and  $\pi$ ) at  $|t_1|/t_2 \gtrsim 2$  as it remains significantly low.

However, the relatively larger value for the regime  $0 < |t_1|/t_2 < 2$  needs more careful interpretation. For instance, in the hard-core boson limit, even in some regions of the dimer phase ( $1 < |t_1|/t_2 < 2$ ),  $\bar{\kappa}_z$  takes a low but finite value. In this case, a relatively higher growth is observed around  $|t_1|/t_2 \approx 1$ , and  $\bar{\kappa}_z$  starts saturating, which indicates the vector chiral ordered phase in the model [82]. Figure 4(b) suggests a similar behavior is observed even when the system is away from the hard-core boson limit, where  $\bar{\kappa}_z$  grows fast and eventually saturates to a high value. We provide a finite-size scaling

of  $\bar{\kappa}_z$  with the system size  $M$  in Figs. 4(c) and (d) for two values of the onsite interaction,  $U = 1$  and  $50$ , respectively. We note that with increasing the system size  $M$ ,  $\bar{\kappa}_z$  tends to converge and the rate of convergence is higher for low values of  $U$ . Moreover, for small  $U$ , even at higher  $M$   $\bar{\kappa}_z$  remains nonzero for almost all considered values of  $|t_1|/t_2$ . In contrast, for large onsite interaction,  $\bar{\kappa}_z$  decreases with increasing system size  $M$  and remains significant only for the region  $|t_1|/t_2 < 2$ .

### C. Dimer order

Further information on the GS behavior can be attained from the dimer order parameters, which can be defined as follows [83, 84],

$$\mathcal{D}_j^{xy} = \frac{1}{2} \langle (\hat{b}_j^\dagger \hat{b}_{j-1} + \hat{b}_{j-1}^\dagger \hat{b}_j) - (\hat{b}_j^\dagger \hat{b}_{j+1} + \hat{b}_{j+1}^\dagger \hat{b}_j) \rangle, \quad (10)$$

and

$$\mathcal{D}_j^{zz} = \langle \left( \frac{1}{2} - \hat{n}_j \right) \left( \frac{1}{2} - \hat{n}_{j-1} \right) - \left( \frac{1}{2} - \hat{n}_{j+1} \right) \left( \frac{1}{2} - \hat{n}_j \right) \rangle. \quad (11)$$

Similar to the chiral order parameter, we define the dimer correlators as

$$\mathcal{D}_{xy}^\Delta = \sum_{j=2}^{M-1-|\Delta|} \langle \mathcal{D}_j^{xy} \mathcal{D}_{j+\Delta}^{xy} \rangle, \quad \mathcal{D}_{zz}^\Delta = \sum_{j=2}^{M-1-|\Delta|} \langle \mathcal{D}_j^{zz} \mathcal{D}_{j+\Delta}^{zz} \rangle, \quad (12)$$

and

$$\bar{\mathcal{D}}_{xy} = \frac{1}{2M-5} \sum_{\Delta=-(M-3)}^{M-3} \frac{\mathcal{D}_{xy}^\Delta}{M-2-|\Delta|},$$

$$\bar{\mathcal{D}}_{zz} = \frac{1}{2M-5} \sum_{\Delta=-(M-3)}^{M-3} \frac{\mathcal{D}_{zz}^\Delta}{M-2-|\Delta|}. \quad (13)$$

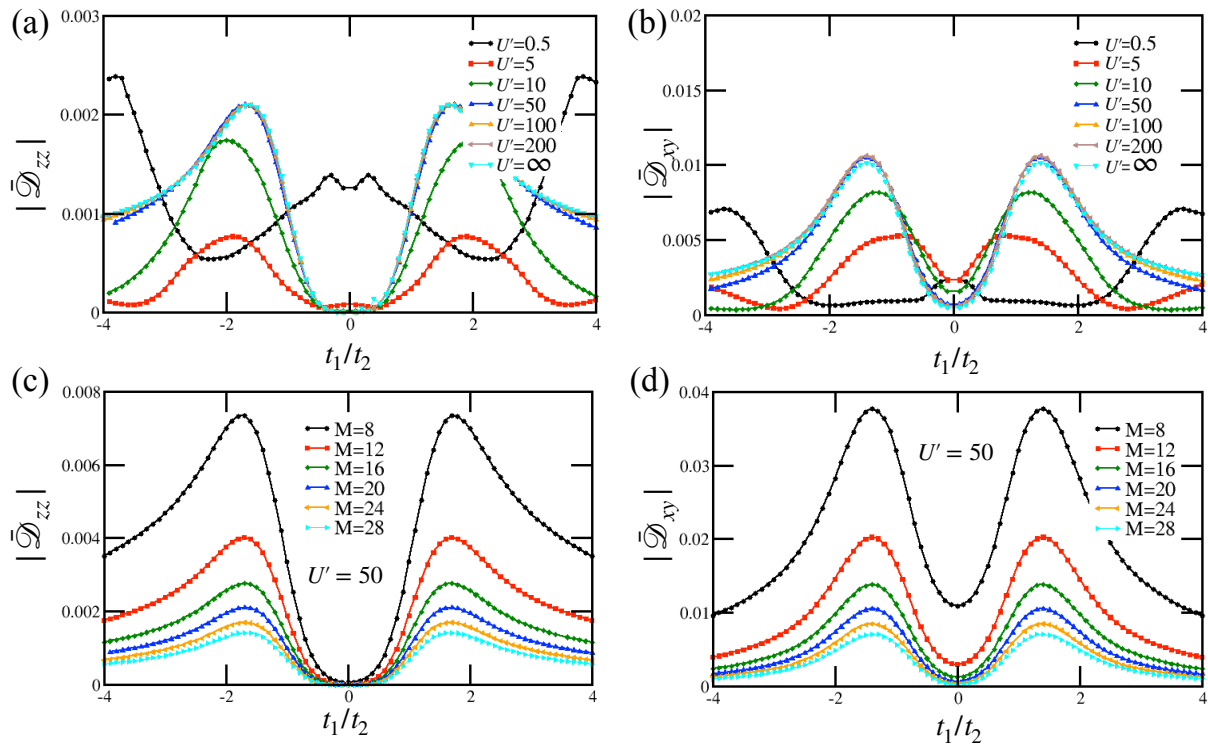


Figure 6. Scaling of dimer correlators with onsite interaction  $U$  and system size  $M$ . Change of (a)  $\bar{\mathcal{D}}_{zz}$  and (b)  $\bar{\mathcal{D}}_{xy}$  with onsite interaction  $U$ , for fixed  $N = 10$ ,  $M = 20$ . (c) and (d), finite-size scaling of both quantities with the system size  $M$  for  $M = 8, 12, 16, 20, 24, 28$ , for fixed  $U' = 50$ . The scaling suggests for large  $M$ , both remain significantly low except for the region with strong quantum fluctuations, i.e.,  $1 < |t_1|/t_2 < 3$ .

We present the behavior of  $\bar{\mathcal{D}}_{zz}$  and  $\bar{\mathcal{D}}_{xy}$  for different values of  $U$  and  $t_1/t_2$  in Figs. 5(a) and (b), respectively. For low values of  $U$ , both quantities remain low for the maximum regions in the considered parameter space, in agreement with an absence of dimer order in that regime. However, relatively high values of both the measures can be observed for a small region around  $q_{\max} \rightarrow 0$  and  $\pi$ .

On the contrary, in the hard-core boson limit, they can be considered as a good identifier of the quantum phase boundaries: in the dimer phase, both quantities attain maximum values, while they remain significantly low for the vector chiral and TLL phases. At high but finite values of  $U$ , the characteristics of both  $\bar{\mathcal{D}}_{zz}$  and  $\bar{\mathcal{D}}_{xy}$  remain similar to that observed for the hard-core boson limit and the GS again possesses finite and high values of dimer correlators for the region  $1 < |t_1|/t_2 < 3$  [see Figs. 6(a) and (b)]. Moreover, similar to vector chiral phase, the quantities remain significantly low in the region  $0 < |t_1|/t_2 < 1$ . The behavior of  $\bar{\mathcal{D}}_{xy}$  and  $\bar{\mathcal{D}}_{zz}$  in the region  $3 < |t_1|/t_2 < 4$  remain intermediate to the previous two regimes. A finite-size scaling for  $U = 50$  [see Figs. 6(c) and (d)] suggests at large  $M$  both the quantities tend to converge in all regions: for  $|t_1|/t_2 < 1$  and  $|t_1|/t_2 > 3$ , they become significantly low. In contrast, for  $1 < |t_1|/t_2 < 3$  both of them possess higher values, indicating strong quantum fluctuations leading to dimerization. We provide analytical forms of the scaling

of both the quantities with the system size  $M$  for the exact dimerization point,  $|t_1|/t_2 = 2$  [see Appendix A], given by

$$\begin{aligned} |\bar{\mathcal{D}}_{zz}| &= \frac{1}{(2M-5)} \frac{M-2}{16(M-3)}, \\ |\bar{\mathcal{D}}_{xy}| &= \frac{1}{8(M-3)}. \end{aligned} \quad (14)$$

For example, for  $M = 20$ , we get  $|\bar{\mathcal{D}}_{zz}| = 0.00189$  and  $|\bar{\mathcal{D}}_{xy}| = 0.00735$ , see Fig. 6(a) and (b). We summarize the behavior of the order parameters obtained above in the schematic Figs. 1(b). In the forthcoming section, we make a comparative study of these findings with the behavior of the entanglement properties in the GS of the system.

#### IV. ENTANGLEMENT PROPERTIES

In this second part of our work, we analyze the behavior of both bipartite and multipartite entanglement obtained for the GS of the model.

##### A. Bipartite entanglement

We start our discussion with the analysis of bipartite entanglement present in the GS of the system. As a mea-

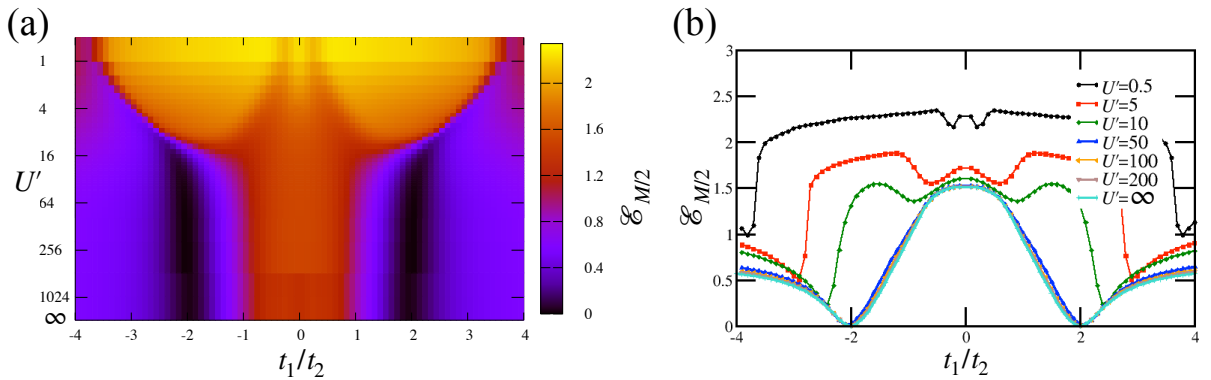


Figure 7. (a) Behavior of half-chain entanglement entropy ( $\mathcal{E}_{M/2}$ ) for  $N = 10$ ,  $M = 20$ . For the same system size, we plot cuts at fixed onsite interaction  $U$  in panel (b). We note that for most of the regions in the considered parameter space, the behavior of  $\mathcal{E}_{M/2}$  remains compatible with  $\bar{\kappa}_z$ . In contrast, at large  $U$ , in the region with strong quantum fluctuations, i.e.,  $1 < |t_1|/t_2 < 3$ , where the dimer orders dominate,  $\mathcal{E}_{M/2}$  remains significantly low. In particular, in the hard-core boson limit at  $|t_1|/t_2 = 2$  GS becomes a product of dimers and  $\mathcal{E}_{M/2}$  is exactly zero.

sure of bipartite entanglement, we consider the half-chain entanglement entropy, defined as

$$\mathcal{E}_{M/2} = -\text{Tr}(\rho \ln \rho), \quad (15)$$

where  $\rho = \text{Tr}_{M/2+1 \dots M}(|\Psi\rangle\langle\Psi|_M)$  is the reduced density matrix consisting of half of the chain, and plot its behavior in Fig. 7(a).

For a large portion of the considered parameter regime, the behavior of bipartite entanglement  $\mathcal{E}_{M/2}$  remains compatible with that of the chiral correlator,  $\bar{\kappa}_z$ , as shown in Fig. 4(a). Similar to  $\bar{\kappa}_z$ ,  $\mathcal{E}_{M/2}$  remains significantly high for low values of contact interaction  $U$  and for almost all values of  $t_1/t_2$  in the considered parameter region. With the increase of  $U$ ,  $\mathcal{E}_{M/2}$  shows interesting behavior. For instance, in the hard-core boson limit, it can distinguish three phases clearly. In the chiral phase ( $|t_1|/t_2 < 1$ ), similar to  $\bar{\kappa}_z$ ,  $\mathcal{E}_{M/2}$  increases monotonically and attains its maximum value. In contrast, for a wide region of the dimer phase ( $1 < |t_1|/t_2 < 3$ )  $\mathcal{E}_{M/2}$  remains considerably low and at the exact dimerization point,  $|t_1|/t_2 = 2$ ,  $\mathcal{E}_{M/2}$  attains its minimum value  $\mathcal{E}_{M/2} = 0$ . In the region  $|t_1|/t_2 > 3$ ,  $\mathcal{E}_{M/2}$  again shows a monotonic growth and saturates to a lower value than that of the chiral phase. Away from the hard-core boson limit, for a finite but large  $U$ , the behavior remains qualitatively similar. This suggests in terms of bipartite entanglement, the phase boundaries obtained for hard-core boson limit translate up to a large but finite  $U$ .

A finite-size scaling analysis in Fig. 8 depicts how  $\mathcal{E}_{M/2}$  scales with system size  $M$  for small [ $U' = 1$ , panel (a) and (b)] and large [ $U' = 50$ , panel (c) and (d)] values of  $U$ . In all the cases,  $\mathcal{E}_{M/2}$  tends to converge fast with the increase of system size  $M$ . For small  $U$ ,  $\mathcal{E}_{M/2}$  remains nonzero for almost all values of  $t_1/t_2$ . At large  $U$ , the same behavior is observed except for the point,  $|t_1|/t_2 = 2$ , and some regions adjacent to that.

## B. Genuine multipartite entanglement

As mentioned previously, in general the computation of multipartite entanglement even for a pure quantum state is a difficult task, and in the literature there exist several inequivalent definitions and measures of it; see, e.g., [58–61, 64]. In our case, we mainly focus on genuine multipartite entanglement (GME) of the system, which is defined as follows. “An  $M$ -party pure quantum state,  $|\Psi\rangle_M$ , is said to be genuinely multipartite entangled if it cannot be written as a product in any possible bipartition of the state”. As a measure of GME, we consider the generalized geometric measure (GGM), which is a computable measure and quantifies the distance of the given  $M$ -party state from the set of states that are not genuinely multipartite entangled. Mathematically, this can be expressed as

$$\mathcal{G}(|\Psi\rangle_M) = 1 - \max_{|\zeta\rangle \in \mathcal{S}_\zeta} |\langle \zeta | \Psi \rangle_M|^2, \quad (16)$$

where  $\mathcal{S}_\zeta$  is the set of states consisting of nongenuinely multipartite entangled states. One can show that an equivalent expression of the above equation is

$$\mathcal{G}(|\Psi\rangle_M) = 1 - \max_{A:B} \lambda_{A:B}^2, \quad (17)$$

where  $\lambda_{A:B}$  is the maximum Schmidt coefficient across the bipartition  $A : B$  with  $A, B \in \{1, 2, \dots, M\}$ ,  $A \cap B = \emptyset$ ,  $A \cup B = M$ , and the maximization has been performed over all possible bipartitions of the state. Because we can decompose any given pure state  $|\Psi\rangle_M$  in Schmidt form and in principle get  $\lambda_{A:B}$  from that, the employed measure does not depend on the dimensionality or underlying lattice structure and can thus be used for a wide range of models, including in higher dimensions [57, 63, 65] or with longer-ranged interactions [66].

We are now ready with the necessary tools to analyze the behavior of GME in the system. Figure 9(a) depicts



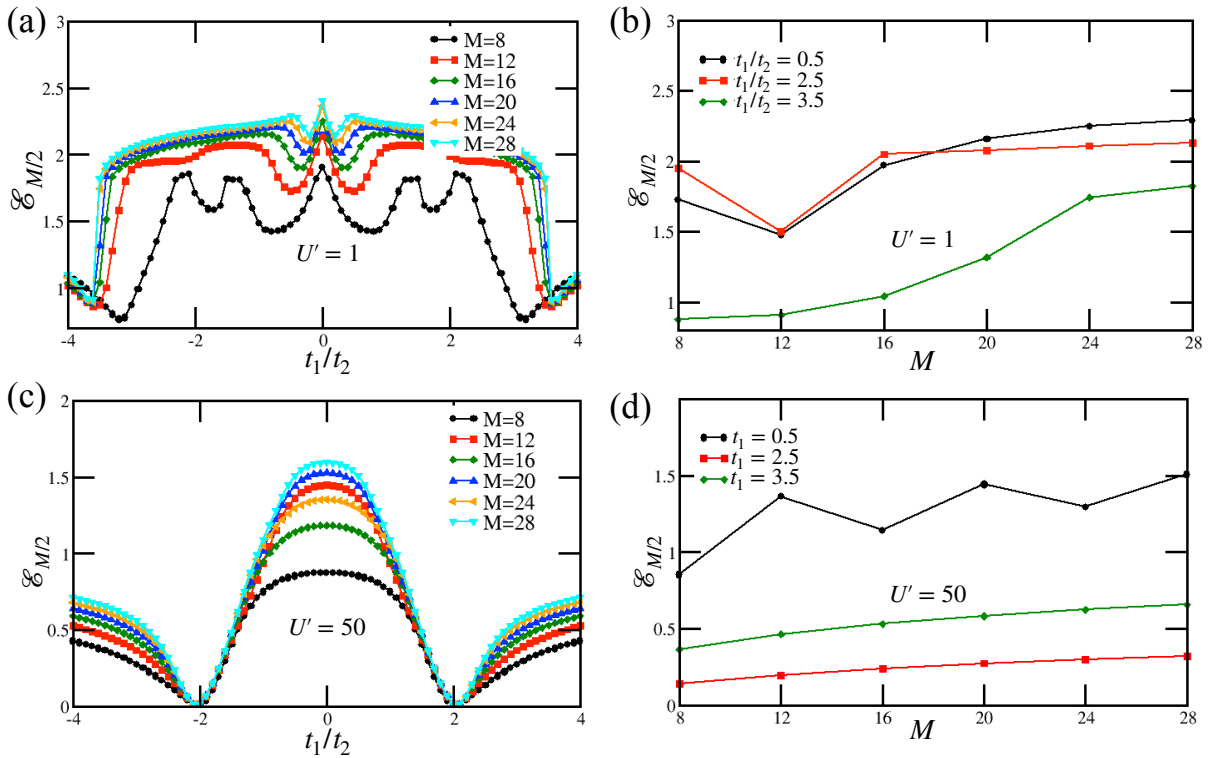


Figure 8. Scaling of  $\mathcal{E}_{M/2}$  with onsite interaction ( $U$ ) and system size ( $M$ ). (a) and (c) depict the scaling of  $\mathcal{E}_{M/2}$  with  $M$  for two values of onsite interactions,  $U = 1$  and  $U = 50$ , respectively. (b) and (d) show a more detailed picture of the rate of convergence of  $\mathcal{E}_{M/2}$  observed in those plots for different values of frustration  $|t_1/t_2|$ . At low  $U$ , bipartite entanglement seems to converge to nonzero values for almost all considered values of  $|t_1/t_2|$ . The same is true when we consider large  $U$ , except for the regions around  $|t_1/t_2| = 2$ .

the behavior of  $\mathcal{G}$  obtained for the GS of the model in the  $U' - t_1/t_2$  plane. From the plot, we note that for low values of onsite interaction and  $|t_1/t_2| > 1$  the behavior of the GME remains characteristically similar to that of the bipartite entanglement and chiral correlator discussed above, and  $\mathcal{G}$  attains a high value. In that region, the optimum value of Schmidt coefficient  $\lambda_{A:B}$  is obtained for contiguous blocks.

In contrast, for  $|t_1/t_2| < 1$ , i.e., when NNN hopping dominates, unlike the previous two quantities,  $\mathcal{G}$  reduces to very low value and the bipartition with  $A \in 2, 4, 6, \dots, N$ , i.e., all even-sites (or equivalently  $B \in 1, 3, 5, \dots, N-1$ , i.e., all odd-sites) yields maximum  $\lambda_{A:B}$ . As the value of onsite interaction is increased further, except for a small region around  $|t_1/t_2| \sim 1$ , the global entanglement shared between the particles remains small in all the regions of the considered parameter space. Similar to bipartite entanglement, for a large fraction of the region with dominating dimer order ( $1 < |t_1/t_2| < 3$ ),  $\mathcal{G}$  remains very low. This suggests in the region where the quantum particles remain maximally spread or delocalized in all the momentum modes, and thus result in a high value of  $\mathcal{S}_q$ , quantum entanglement remains very low or localized. At the exact dimerization point (for  $U \rightarrow \infty$ ),  $|t_1/t_2| = 2$ , where  $\mathcal{S}_q$  is maximum, sim-

ilar to BE, GME also vanishes, as the state separates into a product of dimers. Interestingly, from figure 9(b) we can see that the peak of  $\mathcal{G}$  at  $|t_1/t_2| \approx 0.8$  appears close to the onset point of the vector chiral phase of the model appearing in the hard-core boson limit. However, unlike BE, GME remains low for almost all the regions with dominating chiral correlation ( $|t_1/t_2| < 1$ ), which is very different from the behavior of bipartite entanglement observed in that region. In this region, the system factorizes as  $|\Psi\rangle_M \approx |\phi\rangle_{\text{even sites}} \otimes |\phi\rangle_{\text{odd sites}}$ , and thus multipartite entanglement becomes zero. A finite-size scaling analysis in Fig. 9(c) shows  $\mathcal{G}$  converges with  $M$  fast even for a moderately high value of  $U$ . We summarize the behavior of entanglement properties of the model in the schematic presented in Fig. 1(b).

Therefore, though in some portions of the considered region the behavior of quantum entanglement remains compatible with different order parameters computed for the GS of the system, for a large part of the parameter space, a significant difference can also be observed. In addition to this, depending on the strength of frustration and onsite interaction, even different forms of quantum entanglement (bipartite and multipartite) exhibit distinct behavior. As this shows, the characterization of quantum entanglement in the model demands separate

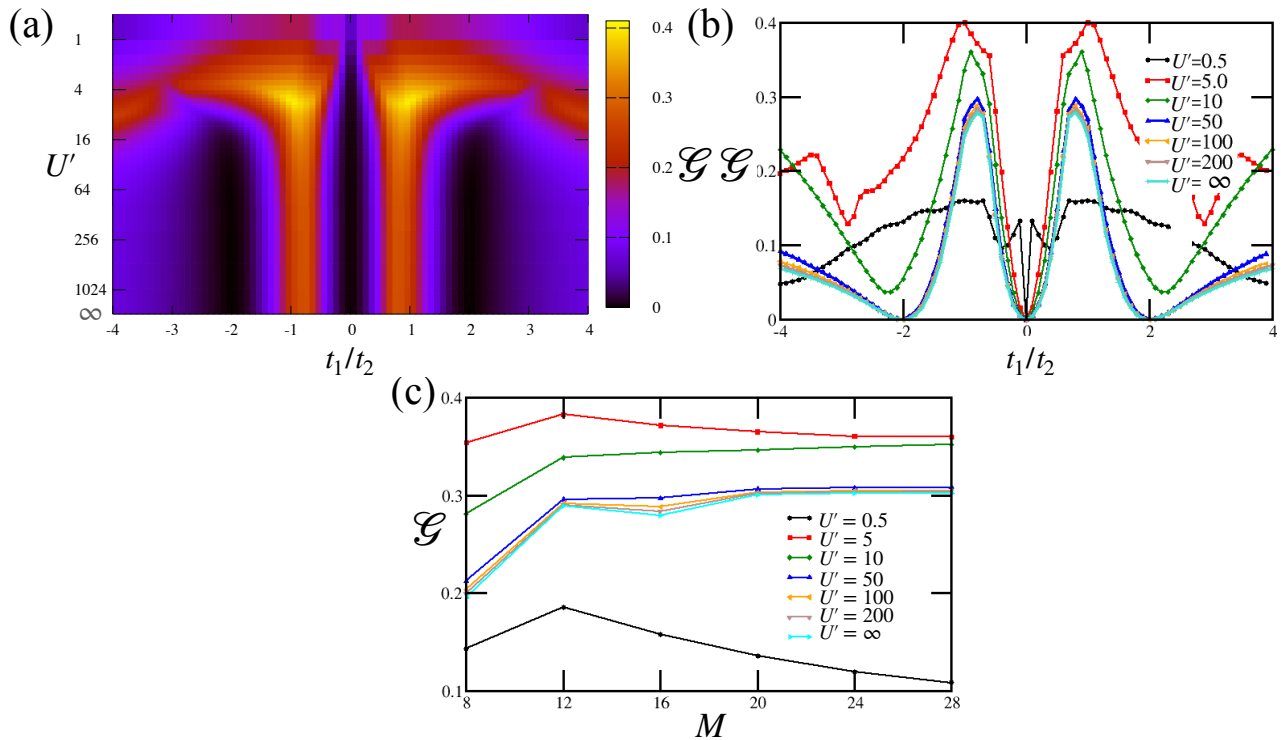


Figure 9. (a) Behavior of generalized geometric measure ( $\mathcal{G}$ ) with onsite interaction and NN and NNN hoppings. Data for  $N = 8$ ,  $M = 16$ . In panel (b), we plot the cuts of  $\mathcal{G}$  against  $U$  for the same system size. For low  $U$ , except for the point  $t_1/t_2 = 0$ ,  $\mathcal{G}$  remains nonzero for the entire considered region. In contrast, for large  $U$ , except for the region adjacent to  $|t_1|/t_2 \approx 1$ ,  $\mathcal{G}$  remains low for almost all values of the considered parameter region. In particular, in the hard-core boson limit  $\mathcal{G}$  becomes zero also at the exact dimerization point  $|t_1|/t_2 = 2$ . Interestingly,  $\mathcal{G}$  attains its peak near  $|t_1|/t_2 \approx 0.8$  which roughly marks the onset point of the vector chiral phase that appears in the hard-core boson limit of the model. Panel (c) shows the scaling of  $\mathcal{G}$  with system size  $M$  (with  $M = 8, 12, 16, 20, 24$ , and  $28$ ), for different  $U$  values at  $t_1/t_2 = 0.8$ . One can see that  $\mathcal{G}$  tends to converge to a finite value with the increase of system size, except for small  $U$ .

attention from the analysis of ordering properties.

## V. CONCLUSION

In this work, we considered the frustrated Bose-Hubbard model with NN and NNN hoppings and examined the quantum properties of the GS of the model. Starting with two limit cases, free bosons and hard-core bosons, we analyzed how different order parameters change with the interplay of frustration and finite onsite interaction. We observed that for the chiral and dimer correlations, the behavior observed in the hard-core boson limit approximately translated up to a moderately large value of  $U$ . Similar behavior was also reported for the population of quantum particles in different momentum modes. We then analyzed the bipartite and multipartite entanglement properties of the system and compared those with the conventional order parameters mentioned above. We found half-chain entanglement entropy remains high for regions with a high value of chiral correlation. However, for the generalized geometric measure, this remains true only for the region with dominating NN

hopping. Along with this, almost all regions with dominating dimer order in the system yield a very low value of both bipartite and genuine multipartite entanglement.

Hence, our analysis reveals that entanglement properties of the system often do not manifest in the behavior of the conventional order parameters computed for the GS of the system and thus deserve separate attention. Moreover, strong quantum fluctuations do not necessarily imply multipartite entanglement. In the present model, e.g., the system resolves strong frustration by tightly binding neighboring sites into dimers and thus due to the monogamy of entanglement, suppressing the distribution of quantum entanglement among a large number of parties.

In the future, it will be interesting to perform similar analyses on other models known for complex quantum mechanical phase diagrams, e.g., those with long-range density-density interactions [79, 95] or frustrated models in two dimensions [88, 96, 97], as well as to compare results to other entanglement measures.

## ACKNOWLEDGMENTS

We acknowledge support by the ERC Starting Grant StrEnQTh (project ID 804305), Provincia Autonoma di Trento, and by Q@TN, the joint lab between University of Trento, FBK-Fondazione Bruno Kessler, INFN-

National Institute for Nuclear Physics and CNR-National Research Council. We thank Soumik Bandyopadhyay for reading the manuscript and providing useful suggestions. We also acknowledge the use of iTensor C++ library for the DMRG computations performed in this work [93].

## Appendix A: Analytical values of dimer correlator for perfect Dimerized state

The perfect triplet dimer for the hard-core limit assumes the form

$$|D\rangle = \prod_{i=1}^{M/2} \left( \frac{\hat{b}_{2k-1}^\dagger + \hat{b}_{2k}^\dagger}{\sqrt{2}} \right) |0\rangle, \quad (\text{A1})$$

where we choose the bonds between the dimers to be between odd-even sites.

We write the single-site dimer order parameter as

$$\hat{\mathcal{D}}_k^{xy} = \left( \hat{j}_k - \hat{j}_{k+1} \right), \quad (\text{A2})$$

where  $\hat{j}_k = \frac{1}{2i} (\hat{b}_k^\dagger \hat{b}_{k-1} + \hat{b}_{k-1}^\dagger \hat{b}_k)$  denotes the current between site  $k$  and site  $k-1$ . With the above dimer form we have the following identities:

$$\langle D | \hat{\mathcal{D}}_k^{xy} \hat{\mathcal{D}}_k^{xy} | D \rangle = -\frac{3}{8}, \quad (\text{A3})$$

$$\langle D | \hat{\mathcal{D}}_k^{xy} \hat{\mathcal{D}}_{k+1}^{xy} | D \rangle = \frac{1}{4} + \frac{1}{8} (k-1 \bmod 2), \quad (\text{A4})$$

$$\langle D | \hat{\mathcal{D}}_k^{xy} \hat{\mathcal{D}}_{k+\Delta}^{xy} | D \rangle = -(-1)^{\Delta \bmod 2} \frac{1}{4}. \quad (\text{A5})$$

This follows

$$\mathcal{D}_{xy}^\Delta = \frac{1}{M-2-|\Delta|} \sum_k \langle \hat{\mathcal{D}}_k^{xy} \hat{\mathcal{D}}_{k+\Delta}^{xy} \rangle = \begin{cases} -\frac{3}{8}, & \text{if } \Delta = 0, \\ \frac{5M-14}{16(M-3)}, & \text{if } |\Delta| = 1, \\ -\frac{1}{4} (-1)^{|\Delta| \bmod 2}, & \text{else.} \end{cases} \quad (\text{A6})$$

Hence, we finally get

$$\begin{aligned} \bar{\mathcal{D}}_{xy} &= \frac{1}{2M-5} \sum_{\Delta=-(M-3)}^{M-3} D_{\Delta}^{xy}, \\ &= \frac{1}{8(M-3)}. \end{aligned} \quad (\text{A7})$$

For the dimer  $zz$  correlator we can proceed as before and obtain

$$\mathcal{D}_{zz}^\Delta = \begin{cases} \frac{1}{8}, & \text{if } \Delta = 0, \\ -\frac{3M-8}{32(M-3)}, & \text{if } |\Delta| = 1, \\ \frac{1}{16} (-1)^{|\Delta| \bmod 2}, & \text{else.} \end{cases} \quad (\text{A8})$$

This implies,

$$\begin{aligned} \bar{\mathcal{D}}_{zz} &= \frac{1}{2M-5} \sum_{\Delta=-(M-3)}^{M-3} D_{\Delta}^{zz}, \\ &= \frac{1}{(2M-5)(M-3)} \left( \frac{2-M}{16} \right). \end{aligned} \quad (\text{A9})$$

- 
- [1] C. H. Bennett and S. J. Wiesner, *Communication via one- and two-particle operators on Einstein-Podolsky-Rosen states*, Phys. Rev. Lett. **69**, 2881 (1992).
- [2] C. H. Bennett, G. Brassard, C. Crépeau, R. Jozsa, A. Peres, and W. K. Wootters, *Teleporting an unknown quantum state via dual classical and Einstein-Podolsky-Rosen channels*, Phys. Rev. Lett. **70**, 1895 (1993).
- [3] P. W. Shor, *Algorithms for quantum computation: Discrete logarithms and factoring*, in Proc. 35th Annu. Symp. Found. Comput. Sci., 124 (1994).
- [4] E. Knill and R. Laflamme, *Power of One Bit of Quantum Information*, Phys. Rev. Lett. **81**, 5672 (1998).
- [5] M. A. Nielsen and I. L. Chuang, *Quantum Computation and Quantum Information* (Cambridge University Press, Cambridge) (2000).
- [6] N. Gisin, G. Ribordy, W. Tittel, and H. Zbinden, *Quantum cryptography*, Rev. Mod. Phys. **74**, 145 (2002).
- [7] R. Horodecki, P. Horodecki, M. Horodecki, and K. Horodecki, *Quantum entanglement* Rev. Mod. Phys. **81**, 865 (2009).
- [8] M. M. Wilde, *Quantum Information Theory* (Cambridge University Press, Cambridge) (2013).
- [9] A. Osterloh, L. Amico, G. Falci, and R. Fazio, *Scaling of entanglement close to a quantum phase transition*, Nature **416**, 608 (2002).
- [10] T. J. Osborne and M.A. Nielsen, *Entanglement in a simple quantum phase transition*, Phys. Rev. A **66**, 032110 (2002).
- [11] L. Amico, R. Fazio, A. Osterloh, and V. Vedral, *Entanglement in many-body systems*, Rev. Mod. Phys. **80**, 517 (2008).
- [12] N. Laflorencie, *Quantum entanglement in condensed matter systems*, Phys. Rep. **646**, 1 (2016).
- [13] B. Zeng, X. Chen, D. L. Zhou, and X. G. Wen, *Quantum Information Meets Quantum Matter: From Quantum Entanglement to Topological Phases of Many-Body Systems* (Quantum Science and Technology) (2021).
- [14] M. Dalmonte and S. Montangero, *Lattice gauge theories simulations in the quantum information era*, Contemporary Physics **57**, 388 (2016).
- [15] M. C. Bañuls, R. Blatt, J. Catani, A. Celi, Juan, I. Cirac, M. Dalmonte, L. Fallani, K. Jansen, M. Lewenstein, S. Montangero, *et al.*, *Simulating lattice gauge theories within quantum technologies*, Eur. Phys. J. D **74**, 165 (2020).
- [16] M. Aidelsburger, L. Barbiero, A. Bermudez, T. Chanda, A. Dauphin, D. González-Cuadra, P. R. Grzybowski, S. Hands, F. Jendrzejewski, J. Jünemann, G. Juzeliūnas, V. Kasper, A. Piga, S.-J. Ran, M. Rizzi, G. Sierra, L. Tagliacozzo, E. Tirrito, T. V. Zache, J. Zakrzewski, E. Zohar, and M. Lewenstein, *Cold atoms meet lattice gauge theory*, Phil. Trans. R. Soc. A **380**, 20210064 (2021).
- [17] V. Panizza, R. C. de Almeida, and P. Hauke, *Entanglement Witnessing for Lattice Gauge Theories*, arXiv:2207.00605 [hep-th] (2022).
- [18] J. M. Maldacena, *The Large  $N$  limit of superconformal field theories and supergravity*, Int. J. Theor. Phys. **38**, 1113 (1999).
- [19] S. Ryu and T. Takayanagi, *Holographic derivation of entanglement entropy from AdS/CFT*, Phys. Rev. Lett. **96**, 181602 (2006).
- [20] G. Vidal, *Entanglement Renormalization*, Phys. Rev. Lett. **99**, 220405 (2007).
- [21] M. V. Raamsdonk, *Building up spacetime with quantum entanglement*, General Relativity and Gravitation **42**, 2323 (2010).
- [22] B. Swingle, *Entanglement renormalization and holography*, Phys. Rev. D **86**, 065007 (2012).
- [23] J. Sonner, *Holographic Schwinger Effect and the Geometry of Entanglement*, Phys. Rev. Lett. **111**, 211603 (2013).
- [24] Th. Sriarunothai, S. Wölk, G. S. Giri, N. Friis, V. Dunjko, H. J. Briegel, P. Kaufmann, T. F. Gloger, D. Kaufmann, M. Johanning, and Ch. Wunderlich, *Quantum Computing with Radiofrequency-driven Trapped Atomic Ions*, in Quantum Information and Measurement (QIM) V: Quantum Technologies, OSA Technical Digest (Optica Publishing Group, 2019), paper S2D.3.
- [25] C. D. Bruzewicz, J. Chiaverini, R. McConnell, and J. M. Sage, *Trapped-Ion Quantum Computing: Progress and Challenges*, Appl. Phys. Rev. **6**, 021314 (2019).
- [26] C. Monroe, W. C. Campbell, L. M. Duan, Z. X. Gong, A. V. Gorshkov, P. W. Hess, R. Islam, K. Kim, N. M. Linke, G. Pagano, P. Richerme, C. Senko, and N. Y. Yao, *Programmable quantum simulations of spin systems with trapped ions*, Rev. Mod. Phys. **93**, 025001 (2021).
- [27] I. Pogorelov, T. Feldker, Ch. D. Marciniak, L. Postler, G. Jacob, O. Krieglsteiner, V. Podlesnic, M. Meth, V. Negnevitsky, M. Stadler, B. Höfer, C. Wöchter, K. Lakhman-

- skiy, R. Blatt, P. Schindler, and T. Monz, *Compact Ion-Trap Quantum Computing Demonstrator*, PRX Quantum **2**, 020343 (2021).
- [28] M. H. Devoret and R. J. Schoelkopf, *Superconducting Circuits for Quantum Information: An Outlook*, Science **339**, 1169 (2013).
- [29] G. Wendin, *Quantum information processing with superconducting circuits: a review*, Rep. Prog. Phys. **80**, 106001 (2017).
- [30] F. Arute, K. Arya, R. Babbush, D. Bacon, J. C. Bardin, R. Barends, R. Biswas, S. Boixo, F. G. S. L. Brandao, D. A. Buell, *et al.* *Quantum supremacy using a programmable superconducting processor*, Nature **574**, 505 (2019).
- [31] P. Jurcevic, A. J. Abhari, L. S. Bishop, I. Laue, I. Lauer, D. F. Bogorin, M. Brink, L. Capelluto, O. Günlük, Toshi-nari Itoko, N. Kanazawa, *et al.*, *Demonstration of quantum volume 64 on a superconducting quantum computing system*, Quantum Sci. Technol. **6**, 025020 (2021).
- [32] F. A. Zwanenburg, A. S. Dzurak, A. Morello, M. Y. Simmons, L. C. L. Hollenberg, G. Klimeck, S. Rogge, S. N. Coppersmith, and M. A. Eriksson, *Silicon quantum electronics*, Rev. Mod. Phys. **85**, 961 (2013).
- [33] M.T. Mądzik, S. Asaad A. Youssry, B. Joecker, K. M. Rudinger, E. Nielsen, K. C. Young, T. J. Proctor, A. D. Baczewski, A. Laucht, V. Schmitt, *et al.*, *Precision tomography of a three-qubit donor quantum processor in silicon*, Nature **601**, 348 (2022).
- [34] X. Xue, M. Russ, N. Samkharadze, B. Undseth, A. Sammak, G. Scappucc, and L. M. K. Vandersypen, *Quantum logic with spin qubits crossing the surface code threshold*, Nature **601**, 343 (2022).
- [35] A. Noiri, K. Takeda, T. Nakajima, T. Kobayashi, A. Sammak, G. Scappucci, and S. Tarucha, *Fast universal quantum gate above the fault-tolerance threshold in silicon*, Nature **601**, 338 (2022).
- [36] D. Bouwmeester, J.W. Pan, K. Mattle, M. Eibl, H. Weinfurter, and A. Zeilinger, *Experimental quantum teleportation*, Nature **390**, 575 (1997).
- [37] F. Flamini, N. Spagnolo and F. Sciarrino, *Photonic quantum information processing: a review*, Rep. Prog. Phys. **82**, 016001 (2019).
- [38] S. Azzini, S. Mazzucchi, V. Moretti, D. Pastorello, and L. Pavesi, *Single-particle entanglement*, Advanced Quantum Technologies, **3** **10**, 2000014 (2020).
- [39] H. S. Zhong, H. Wang, Y.H. Deng, M. C. Chen, *Quantum computational advantage using photons*, Science **370**, 1460 (2020).
- [40] F. Xu, X. Ma, Q. Zhang, H. K. Lo, J. W. Pan, *Secure quantum key distribution with realistic devices*, Rev. Mod. Phys. **92**, 025002 (2020).
- [41] L. S. Madsen, F. Laudenbach, M. F. Askarani, F. Rortais, T. Vincent, J. F. F. Bulmer, F. M. Miatto, L. Neuhaus, Lukas G. Helt, M. J. Collins, A. E. Lita, *et al.*, *Quantum computational advantage with a programmable photonic processor*, Nature **606**, 75 (2022).
- [42] M. Lewenstein, A. Sanpera, V. Ahufinger, B. Damski, A. Sen(De), and U. Sen, *Ultracold atomic gases in optical lattices: mimicking condensed matter physics, and beyond* Adv. Phys. **56**, 24 (2007).
- [43] M. Saffman, T. G. Walker, and K. Mølmer, *Quantum information with Rydberg atoms*, Rev. Mod. Phys. **82**, 2313 (2010).
- [44] L. Henriot, L. Beguin, A. Signoles, T. Lahaye, A. Browaeys, G. O. Reymond, and C. Jurczak, *Quantum computing with neutral atoms*, Quantum **4**, 327 (2020).
- [45] I. Bloch, *Quantum coherence and entanglement with ultracold atoms in optical lattices*, Nature **453**, 1016 (2008).
- [46] M. Riedel, P. Böhi, Y. Li, T. W. Hänsch, A. Sinatra, and P. Treutlein, *Atom-chip-based generation of entanglement for quantum metrology*, Nature **464**, 1170 (2010).
- [47] P. Jurcevic, B. P. Lanyon, P. Hauke, C. Hempel, P. Zoller, R. Blatt, and C. F. Roos, *Quasiparticle engineering and entanglement propagation in a quantum many-body system*, Nature **511**, 202 (2014).
- [48] N. Friis, O. Marty, C. Maier, C. Hempel, M. Holzöpfel, P. Jurcevic, M. B. Plenio, M. Huber, C. Roos, R. Blatt, and B. Lanyon, *Observation of Entangled States of a Fully Controlled 20-Qubit System*, Phys. Rev. X **8**, 021012 (2018).
- [49] M. Gong, M. C. Chen, Y. Zheng, S. Wang, C. Zha, H. Deng, Z. Yan, H. Rong, Y. Wu, S. Li, F. Chen, *et al.*, *Genuine 12-Qubit Entanglement on a Superconducting Quantum Processor*, Phys. Rev. Lett. **122**, 110501 (2019).
- [50] F. Verstraete, M. A. Martín-Delgado, and J. I. Cirac, *Diverging Entanglement Length in Gapped Quantum Spin Systems*, Phys. Rev. Lett. **92**, 087201 (2004).
- [51] F. Verstraete, M. Popp, and J. I. Cirac, *Entanglement versus Correlations in Spin Systems*, Phys. Rev. Lett. **92**, 027901 (2004).
- [52] L. A. Wu, M. S. Sarandy, and D. A. Lidar, *Quantum Phase Transitions and Bipartite Entanglement*, Phys. Rev. Lett. **93**, 250404 (2004).
- [53] S. M. Giampaolo, G. Adesso, and F. Illuminati, *Probing Quantum Frustrated Systems via Factorization of the Ground State*, Phys. Rev. Lett. **104**, 207202 (2010).
- [54] G. De Chiara, L. Lepori, M. Lewenstein, and A. Sanpera, *Entanglement Spectrum, Critical Exponents, and Order Parameters in Quantum Spin Chains*, Phys. Rev. Lett. **109**, 237208 (2012).
- [55] M. Hofmann, A. Osterloh, and O. Gühne, *Scaling of genuine multiparticle entanglement close to a quantum phase transition*, Phys. Rev. B **89**, 134101 (2014).
- [56] P. Hauke, M. Heyl, L. Tagliacozzo, and P. Zoller, *Measuring multipartite entanglement through dynamic susceptibilities*, Nat. Phys. **12**, 778 (2016).
- [57] S. Singha Roy, H.S. Dhar, D. Rakshit, A. Sen De, and U. Sen, *Detecting phase boundaries of quantum spin-1/2 XXZ ladder via bipartite and multipartite entanglement transitions*, J. Magn. Magn. Mater **444**, 227 (2017).
- [58] T. C. Wei and P. M. Goldbart, *Geometric measure of entanglement and applications to bipartite and multipartite quantum states*, Phys. Rev. A **68**, 042307 (2003).
- [59] M. Blasone, F. Dell'Anno, S. DeSiena, and F. Illuminati, *Hierarchies of geometric entanglement*, Phys. Rev. A **77**, 062304 (2008).
- [60] A. Sen(De) and U. Sen, *Channel capacities versus entanglement measures in multiparty quantum states*, Phys. Rev. A **81**, 012308 (2010).
- [61] A. Sen(De) and U. Sen, *Bound Genuine Multisite Entanglement: Detector of Gapless-Gapped Quantum Transitions in Frustrated Systems*, arXiv:1002.1253 [quant-ph].
- [62] S. Singha Roy, H. S. Dhar, D. Rakshit, A. Sen(De), and U. Sen, *Diverging scaling with converging multisite entanglement in odd and even quantum Heisenberg ladders*, New J. Phys., **18** 023025 (2016).
- [63] S. Singha Roy, H. S. Dhar, D. Rakshit, A. Sen(De), and U. Sen, *Analytical recursive method to ascertain multisite*

- entanglement in doped quantum spin ladders*, Phys. Rev. B **96**, 075143 (2017).
- [64] G. De Chiara and A. Sanpera, Genuine quantum correlations in quantum many-body systems: a review of recent progress, Rep. Prog. Phys. **81**, 074002 (2018).
- [65] S. Singha Roy, H. S. Dhar, D. Rakshit, A. Sen(De), and U. Sen, *Response to defects in multipartite and bipartite entanglement of isotropic quantum spin networks*, Phys. Rev. A **97**, 052325 (2018).
- [66] S. Singha Roy and H. S. Dhar, *Effect of long-range interactions on multipartite entanglement in Heisenberg chains*, Phys. Rev. A **99**, 062318 (2019).
- [67] S. Singha Roy, H. S. Dhar, A. Sen(De), and U. Sen, *Tensor-network approach to compute genuine multisite entanglement in infinite quantum spin chains*, Phys. Rev. A **99**, 062305 (2019).
- [68] A. Bera and S. Singha Roy, *Growth of genuine multipartite entanglement in random unitary circuits*, Phys. Rev. A **102**, 062431 (2020).
- [69] H. J. Briegel, D. E. Browne, W. Dür, R. Raussendorf, and M. Van den Nest, *Measurement-based quantum computation*, Nature Phys **5**, 19 (2009).
- [70] M. Epping, H. Kampermann, C. Macchiavello, and D. Bruß, *Multi-partite entanglement can speed up quantum key distribution in networks*, New J. Phys. **19**, 093012 (2017).
- [71] Q. Zhuang, Z. Zhang, and J. H. Shapiro, *Distributed quantum sensing using continuous-variable multipartite entanglement*, Phys. Rev. A **97**, 032329 (2018).
- [72] L. Pezzè, A. Smerzi, M. K. Oberthaler, R. Schmied, and P. Treutlein, *Quantum metrology with nonclassical states of atomic ensembles*, Rev. Mod. Phys. **90**, 035005 (2018).
- [73] A. J. Scott, *Multipartite entanglement, quantum-error-correcting codes, and entangling power of quantum evolutions*, Phys. Rev. A **69**, 052330 (2004).
- [74] S. M. Giampaolo and B. C. Hiesmayr, *Genuine multipartite entanglement in the cluster-Ising model*, New J. Phys. **16**, 093033 (2014).
- [75] T. R. de Oliveira, G. Rigolin, and M. C. de Oliveira, *Genuine multipartite entanglement in quantum phase transitions*, Phys. Rev. A **73**, 010305(R) (2006).
- [76] S. Haldar, S. Roy, T. Chanda, A. Sen(De), and U. Sen, *Multipartite entanglement at dynamical quantum phase transitions with nonuniformly spaced criticalities*, Phys. Rev. B **101**, 224304 (2020).
- [77] Z. H. Ma, Z. H. Chen, J. L. Chen, C. Spengler, A. Gabriel, and M. Huber, *Measure of genuine multipartite entanglement with computable lower bounds*, Phys. Rev. A **83**, 062325 (2011).
- [78] J. Hubbard, *Electron correlations in narrow energy bands*, Phys. Rev. B, **17**, 494 (1978).
- [79] O. Dutta, M. Gajda, P. Hauke, M. Lewenstein, D. S. Lühmann<sup>8</sup>, B. A. Malomed, T. Sowiński<sup>2</sup>, and J. Zakrzewski, *Non-standard Hubbard models in optical lattices: a review*, Rep. Prog. Phys. **78**, 066001 (2015).
- [80] E. Anisimovas, M. Račiūnas, C. Sträter, A. Eckardt, I. B. Spielman, and G. Juzeliūnas *Semisynthetic zigzag optical lattice for ultracold bosons*, Phys. Rev. A **94**, 063632 (2016).
- [81] C K Majumdar and D Ghosh, *On Next-Nearest-Neighbor Interaction in Linear Chain*, J. Math. Phys. **10**, 1388 (1969).
- [82] R. Schmied, T. Roscilde, V. Murg, D. Porras, and J. I. Cirac, *Quantum phases of trapped ions in an optical lattice*, New J. Phys. **10**, 045017 (2008).
- [83] M. Sato, S. Furukawa, S. Onoda, and A. Furusaki, *Competing phases in spin-1/2 J1-J2 chain with easy-plane anisotropy*, Mod. Phys. Lett. B Vol. **25**, 901 (2011).
- [84] S. Furukawa, M. Sato, S. Onoda, and A. Furusaki, *Ground-state phase diagram of a spin-1/2 frustrated ferromagnetic XXZ chain: Haldane dimer phase and gapped/gapless chiral phases*, Phys. Rev. B **86**, 094417 (2012).
- [85] J. Cabedo, J. Claramunt, J. Mompart, V. Ahufinger, and A. Celi, *Effective triangular ladders with staggered flux from spin-orbit coupling in 1D optical lattices*, Eur. Phys. J. D **74**, 123 (2020).
- [86] A. Eckardt, C. Weiss, and M. Holthaus, *Superfluid-Insulator Transition in a Periodically Driven Optical Lattice*, Phys. Rev. Lett. **95**, 260404 (2005).
- [87] H. Lignier, C. Sias, D. Ciampini, Y. Singh, A. Zenesini, O. Morsch, and E. Arimondo, *Dynamical Control of Matter-Wave Tunneling in Periodic Potentials*, Phys. Rev. Lett. **99**, 220403 (2007).
- [88] A. Eckardt, P. Hauke, P. Soltan-Panahi, C. Becker, K. Sengstock, and M. Lewenstein, *Frustrated quantum anti-ferromagnetism with ultracold bosons in a triangular lattice*, Euro. Phys. Lett. **89**, 10010 (2010).
- [89] J. Struck, C. Ölschläger, R. Le Targat, P. S. Panahi, A. Eckardt, M. Lewenstein, P. Windpassinger, and K. Sengstock, *Quantum simulation of frustrated classical magnetism in triangular optical lattices*, Science **6045**, 996 (2011).
- [90] J. Dalibard, F. Gerbier, G. Juzeliūnas, and P. Öhberg, *Colloquium: Artificial gauge potentials for neutral atoms*, Rev. Mod. Phys. **83**, 1523 (2011).
- [91] P. Hauke and I. Carusotto, *Quantum Hall and Synthetic Magnetic-Field Effects in Ultra-Cold Atomic Systems*, arXiv:2206.07727 [cond-mat.quant-gas] (2022).
- [92] T. Holstein and H. Primakoff, *Field Dependence of the Intrinsic Domain Magnetization of a Ferromagnet*, Phys. Rev. **58**, 1098 (1940).
- [93] M. Fishman and S. R. White and E. Miles Stoudenmire, *The ITensor Software Library for Tensor Network Calculations*, arXiv:2007.14822 [cs.MS] (2020).
- [94] T. Hikihara, M. Kaburagi, H. Kawamura, and T. Tonegawa, *Exact Ground States of Frustrated Quantum Spin Systems Consisting of Spin-Dimer Units*, J. Phys. Soc. Jpn. **69**, 259 (2000).
- [95] X. Deng, G. Masella, G. Pupillo, and L. Santos, *Universal Algebraic Growth of Entanglement Entropy in Many-Body Localized Systems with Power-Law Interactions*, Phys. Rev. Lett. **125**, 010401 (2020).
- [96] G. Misguich and C. Lhuillier, *Two-dimensional quantum antiferromagnets*, Frustrated Spin Systems, 229 (2005).
- [97] B. Schmidt and P. Thalmeier, *Frustrated two dimensional quantum magnets*, Physics Reports **703**, 1 (2017).